A Nanoscale Optical Biosensor: The Long Range Distance Dependence of the Localized Surface Plasmon Resonance of Noble Metal Nanoparticles

Amanda J. Haes, Shengli Zou, George C. Schatz, and Richard P. Van Duyne*

Contributions from the Department of Chemistry, Northwestern University, Evanston, Illinois 60208-3113

Received: July 21, 2003; In Final Form: September 26, 2003

The elucidation of the long range distance dependence of the localized surface plasmon resonance (LSPR) of surface-confined noble metal nanoparticles is the aim of this work. It was suspected that the linear distance dependence found in $CH_3(CH_2)_xSH$ self-assembled monolayer (SAM) formation was the thin shell limit of a longer range, nonlinear dependence. To verify this, multilayer SAM shells based on the interaction of $HOOC(CH_2)_{10}SH$ and Cu^{2+} were assembled onto surface-confined noble metal nanoparticles and were monitored using UV−visible spectroscopy. Measurement of the LSPR extinction peak shift versus number of layers and adsorbate thickness is nonlinear and has a sensing range that is dependent on the composition, shape, in-plane width, and out-of-plane height of the nanoparticles. Theoretical calculations based on an accurate electrodynamics description of the metal nanoparticle plus surrounding layered material indicate plasmon resonance wavelength shifts that are in excellent agreement with the measurements. The calculations show that the sensing range is determined by falloff of the average induced electric field around the nanoparticle. This detailed set of experiments coupled with an excellent theory versus experiment comparison prove that the sensing capabilities of noble metal nanoparticles can be size tuned to match the dimensions of biological and chemical analytes by adjusting the aforementioned properties. The optimization of the LSPR nanosensor for a specific analyte will significantly improve an already sensitive nanoparticle-based sensor.

I. Introduction

Advancements in technology because of nanoscale phenomena will be made and optimized when the chemical and physical properties of materials are more thoroughly understood.[1−8] Prior to the realization of these properties, methods to synthesize monodisperse nanoparticles and to isolate them in a controlled environment are two obstacles that must be overcome.

The development of nanoparticle-based optical sensors is an extremely active area of nanoscience research.[9−14] One such optical nanoparticle based sensor is known as the localized surface plasmon resonance (LSPR) nanosensor. The LSPR of noble metal nanoparticles arises when electromagnetic radiation induces a collective oscillation of the conduction electrons of the individual nanoparticles[15−23] and has two primary consequences: (1) selective photon absorption which allows the optical properties of these nanoparticles to be monitored with UV−vis spectroscopy and (2) the enhancement of the electromagnetic fields surrounding the nanoparticles which is responsible for all surface-enhanced spectroscopies.

Previously, it has been shown that the LSPR of nanoparticles synthesized using nanosphere lithography (NSL) creates homogeneous surface-confined nanotriangles.[15,24] Additionally, the LSPR extinction wavelength maxima of these nanoparticles can be systematically tuned by changing their shape and size.[25] More notably, the Ag nanotriangles are extremely sensitive to their dielectric environment and, therefore, behave as sensitive nanosensors.[26−28] For Ag nanotriangles with in-plane widths (a) = 100 nm and out-of-plane heights (b) = 50.0 nm, their sensing capabilities have been demonstrated via five pathways. First, the refractive index sensitivity of Ag nanotriangles is approximately 1 part in 100.[26] Second, the sensitivity of Ag nanotriangles to self-assembled monolayers (SAMs) composed of alkanethiols ($CH_3(CH_2)_xSH$, $x = 3-15$) is linear and shifts ∼3.3 nm per methylene group with a negative intercept of 8.5 which arises from the Ag−S charge-transfer interaction.[26] Third, it was shown that poly-(L)-lysine could reversibly bind to Ag nanoparticles.[26] Fourth, by studying the concentration effects of streptavidin onto biotinylated Ag nanotriangles, it was displayed that the surface-confined binding constant of this system was $\sim 1 \times 10^{11}$ M^{-1} with a limit of detection (LOD) less than 1 pM.[27] In that same study, it was shown that the nonspecific binding interactions of the system are minimal.[27] Finally, the antigen−antibody interaction of biotin to antibiotin had a surface-confined binding constant of 4.5×10^7 M^{-1} and an LOD less than 100 pM.[28] Additionally, it was shown that this interaction is reversible and could be monitored in buffer.[28]

Recently, McFarland and Van Duyne demonstrated that single Ag nanoparticles can be used to sense local refractive index changes induced via bulk solvent changes and a monolayer of alkanethiols.[29] Specifically, using dark-field microscopy, the LSPR extinction maximum response of individual Ag nanoparticles to the adsorption of less than 60 000 hexadecanethiol molecules is ∼40 nm. Additionally, kinetic responses were monitored and were competitive with other real-time sensors. Through this work and the single Au nanoparticle work by Rashke et al.,[30] it has been demonstrated that the detection limits of the nanoparticle array based sensor can be dramatically decreased using individual nanoparticles.

All aforementioned LSPR binding experiments were performed without the consideration of nanoparticle composition, shape, or size. For this reason, the short range distance dependence of LSPR nanosensors was studied by varying the

* Corresponding author. E-mail: vanduyne@chem.northwestern.edu.

10.1021/jp0361327 CCC: $27.50
Published on Web 12/05/2003

nanoparticles' composition, shape, and size.[27] The short range distance dependence for a single adsorbate, hexadecanethiol, was most sensitive for nonhemispherical, Ag (vs Au) and small aspect ratio nanoparticles. Given the length of hexadecanethiol (~2.61 nm),[31] this effect was attributed to varying electromagnetic field strength, induced by their LSPR, at the surface of the nanoparticles. The study, however, did not probe the electromagnetic field strength, also known as the overall sensing volume of the nanoparticles, a given distance from the nanoparticle surface.

Several different layer-by-layer self-assembly strategies have been demonstrated: cationic and anionic colloidal particles,[32] oppositely charged polyelectrolytes,[33−36] and polyelectrolytes to clay platlets,[37−41] graphite oxide platlets,[42] zirconium phosphate platelets,[43] colloidal metal particles,[44,45] or colloidal semiconductor particles.[41] These assemblies are recognized as a valid method for the construction of two-dimensional and three-dimensional networks. The formation of multilayer structures using metal ion association to a carboxylated surface[46−50] offers another controlled molecular interaction of these multilayer films to nanostructures for photolithographic patterning.

The metal ion, carboxylated alkanethiol SAM has many desirable characteristics:[49,50] (1) the first alkanethiol layer forms with the thiol group on the metal surface with no significant mixing of molecule orientation, (2) the second (and additional) alkanethiol layer forms with the same orientation as the first, (3) the first two alkanethiol layers have approximately equal number of molecules, (4) 20+ uniform layers can be formed, and (5) the refractive index of the layer is constant and assumed to be ~1.5 to 1.6 depending on layer ordering.[50,51] The exact binding of alkanethiols to the metal ions is unclear. X-ray photoelectron spectroscopy studies indicate that one to eight metal ions coordinate to every two carboxyl groups. Despite this unknown interaction, this multilayer structure offers a simple, controlled way to probe the long-range distance dependence, and correspondingly, the electromagnetic field strength 10+ nm away from the nanostructured surfaces.[46]

In this study, the long range LSPR distance dependence of noble metal nanoparticles will be probed using multilayer formation of 11-mercaptoundecanoic acid and Cu^{2+} ions. The following long-range aspects of the LSPR nanosensor will be demonstrated: (1) the LSPR shift versus number of adsorbate layers and adsorbate thickness is nonlinear; (2) despite differences of SAM orientation on Au versus Ag, Ag nanotriangles are more sensitive, that is, produce larger extinction peak shifts for a given multilayer thickness and a larger sensing volume than Au nanotriangles; (3) nanotriangles have larger sensing volumes and are more sensitive to multilayer adsorbates than nanohemispheres of equal volume; (4) larger nanoparticle widths for a given nanotriangle height reveal larger LSPR sensing volumes; and (5) smaller nanoparticle heights for a given nanoparticle width reveal larger LSPR sensing volumes. Finally, a semi-quantitative theoretical interpretation of these responses will be offered. These features clearly demonstrate that the long range distance dependence of noble metal nanoparticles is shape and size tunable. These characteristics indicate that the sensing capabilities of noble metal nanoparticles can be refined to produce more sensitive biological and chemical sensors.

II. Experimental and Methods

Materials. 11-Mercaptoundecanoic acid (11-MUA) and $Cu(ClO_4)_2$ were purchased from Aldrich (Milwaukee, WI). Absolute ethanol was purchased from Pharmco (Brookfield, CT). Hexanes and methanol were purchased from Fisher Scientific (Pittsburgh, PA). Ag wire (99.99%, 0.5 mm diameter) and Au wire (99.9%, 0.025 mm diameter) were obtained from D. F. Goldsmith (Evanston, IL). Borosilicate glass substrates, No. 2 Fisherbrand 18 mm circle coverslips were purchased from Fisher Scientific (Pittsburgh, PA). Tungsten vapor deposition boats were acquired from R. D. Mathis (Long Beach, CA). Polystyrene nanospheres with diameters of 280 ± 4 nm, 310 ± 9 nm, 400 ± 8 nm, 450 ± 5 nm, and 510 ± 11 nm were received as a suspension in water (Interfacial Dynamics Corporation, Portland, OR) and were used without further treatment. Millipore cartridges (Marlborough, MA) were used to purify water to a resistivity of 18 $M\Omega cm^{-1}$. All materials were used without further purification.

Substrate Preparation. Glass substrates were cleaned in a piranha solution (1:3 30% H_2O_2:H_2SO_4) at 80 °C for 30 min. Once cooled, the glass substrates were rinsed with copious amounts of water and then sonicated for 60 min in 5:1:1 H_2O:NH_4OH:30% H_2O_2. Next, the glass was rinsed repeatedly with water and was stored in water until used.

Nanoparticle Preparation. NSL was used to fabricate monodisperse, surface-confined Ag nanoparticles.[15,24] For these experiments, single-layer colloidal crystal nanosphere masks were prepared by drop coating ~2 μL of nanosphere solution onto glass substrates. Once the nanosphere masks were dry, the substrates were mounted into a Consolidated Vacuum Corporation vapor deposition system. A Leybold Inficon XTM/2 quartz crystal microbalance (East Syracuse, NY) was used to measure the thickness of the Ag or Au film deposited over the nanosphere mask, d_m. Following metal deposition, the nanosphere mask was removed by sonicating the sample in ethanol for 3 min. The perpendicular bisector of the nanoparticles, a, was varied by changing the diameter, D, of the nanospheres used. The samples were either thermally annealed for 1 h at ~600 °C in the aforementioned chamber or solvent annealed. Unless otherwise noted, all samples were stabilized by solvent annealing. While the solvent slightly restructures the nanoparticles, that is, causes slight rounding of the nanotriangle tips, the overall triangular footprint is retained, and in this process, also produces stable extinction maxima readings in a given environment. Thermal annealing is performed to convert the nanotriangles into nanohemispheres. A comparison between the two annealing methods enables the study of LSPR sensing as a function of nanoparticle shape.

Ultraviolet−Visible Extinction Spectroscopy. Macroscale UV−vis extinction measurements were collected using an Ocean Optics (Dunedin, FL) SD2000 fiber optically coupled spectrometer with a CCD detector. All spectra collected are macroscopic measurements performed in standard transmission geometry with unpolarized light. The probe beam diameter was approximately 4 mm.

Nanoparticle Annealing. A home-built flow cell[26] was used to control the external environment of the Ag nanoparticle substrates. Prior to modification, the Ag nanoparticles were solvent annealed[26] with hexanes and methanol. Dry N_2 gas and solvent were cycled through the flow cell until the λ_{max} of the sample stabilized. After incubation, the nanoparticle samples were rinsed with ethanol and dried by flowing N_2 gas through the sample cell.

Nanoparticle Functionalization. After solvent annealing, the nanoparticle samples were functionalized with 1 mM 11-MUA (ethanol) solutions. Within 10 min, the extinction maximum of the sample stabilized and the sample was rinsed with copious amounts of ethanol. Next, a 1 mM $Cu(ClO_4)_2$ (ethanol) was exposed to the sample until the extinction maximum peak had

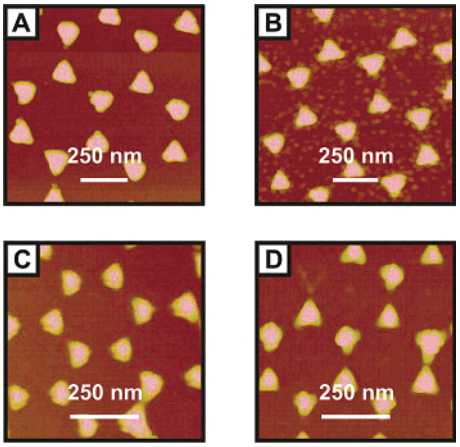

Figure 1. Representative tapping mode AFM images of nanoparticles. Scan rate = 2.0 Hz. (A) Ag nanoparticles (nanoparticle width, a = 100 nm, nanoparticle height, b = 50.0 nm) before incubation in HS−$(CH_2)_{10}$–COOH/Cu^{2+} and (B) after incubation in two layers of HS−$(CH_2)_{10}$−COOH/Cu^{2+}. Average layer thickness = 1.6 nm. Scan areas ~1 μm^2. The particulate features seen on this image are of unknown origins but highly reproducible. (C) Au nanoparticles (a = 70 nm, b = 50 nm) before incubation in HS−$(CH_2)_{10}$−COOH/Cu^{2+} and (D) after incubation in two layers of HS−$(CH_2)_{10}$−COOH/Cu^{2+}. Average layer thickness = 1.4 nm. Scan areas ~0.5 μm^2.

stabilized (less than 3 min). The sample cell was flushed with ethanol, and the extinction spectrum of the sample in N_2 was collected. The previous steps were repeated until the extinction maximum no longer shifted with functionalization.

Atomic Force Microscopy (AFM). AFM images were collected using a Digital Instruments Nanoscope IV microscope and Nanoscope IIIa controller operating in tapping mode. Etched Si nanoprobe tips (TESP, Digital Instruments, Santa Barbara, CA) were used. These tips had resonance frequencies between 280 and 320 kHz and are conical in shape with a cone angle of 20° and an effective radius of curvature at the tip of 10 nm. All images shown here are unfiltered data that were collected in ambient conditions. The height of the nanoparticles, b, was determined using AFM.

III. Results and Discussion

AFM and Optical Interpretation of Multilayers on NSL Derived Nanoparticles. NSL was used to synthesize Ag and Au nanoparticles on glass substrates. Representative AFM images of Ag nanoparticles before and after incubation in two layers of 11-MUA/Cu^{2+} are found in Figure 1A and 1B, respectively. The particulate features in Figure 1B are of unknown but highly reproducible origins. Their presence does not affect our conclusions. Representative AFM images of Au nanoparticles before and after incubation in two layers of 11−MUA/Cu^{2+} are found in Figure 1C and 1D, respectively. As determined by AFM linescans, average thickness per SAM layer is 1.6 nm for Ag and 1.4 nm for Au. These values were obtained from 30+ nanoparticles that had been incubated in 1−15 SAM layers.

The UV−vis extinction spectra for Ag nanoparticles (a = 100 nm, b = 50 nm) and Au nanoparticles (a = 70 nm, b = 50 nm) with 0−20 SAM layers are found in Figure 2A and 2B, respectively. Several distinctive features can be discerned from these data. As the adsorbate layer thickness increases, the extinction maximum red shifts, the full width half-maximum (FWHM) remains approximately constant (100 ± 10 nm), and the peak intensity increases. At some point (for the Ag nanoparticle case), at layer 18, the extinction maximum stops

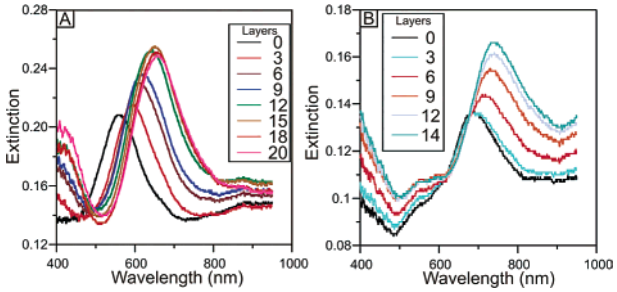

Figure 2. Long range LSPR spectroscopy of (A) Ag nanoparticles (a = 100 nm, b = 50.0 nm) for 0−20 layers of Cu^{2+}/HS−$(CH_2)_{10}$COOH (B) Au nanoparticles (a = 70 nm, b = 50.0 nm) for 0−14 layers of Cu^{2+}/HS−$(CH_2)_{10}$COOH. All extinction measurements were collected in a N_2 environment.

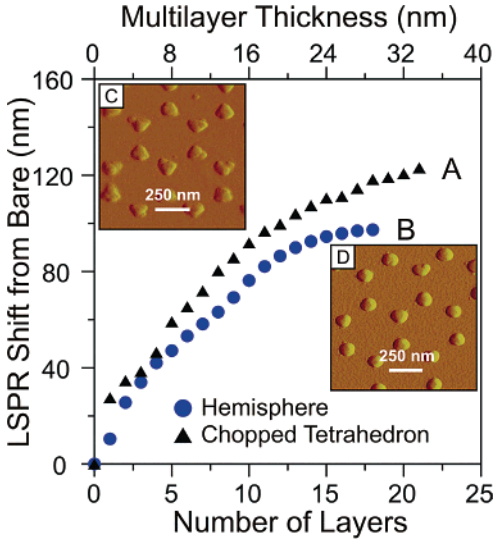

Figure 3. Shape dependence on the long range LSPR distance dependence for Ag nanoparticles (D = 400 nm). (A) LSPR shift vs number of SAM layer thickness for solvent annealed Ag nanoparticles. (B) LSPR shift vs number of SAM layer thickness for thermally annealed (600 °C for 1 h) Ag nanoparticles. (C) AFM image of solvent annealed nanoparticles (a = 114 nm, b = 54 nm). (D) AFM image of thermally annealed nanoparticles (a = 110 nm, b = 61 nm). All extinction measurements were collected in a N_2 environment.

shifting, the FWHM begins increasing, and the peak intensity begins to decrease. These three diagnostic features signal that of the sensing volume of the nanoparticle had been saturated.

Shape Influences on the LSPR Shifts Induced by Multilayer Adsorbates. An example of the LSPR extinction maximum shift from bare nanotriangles and nanohemispheres versus multilayer thickness (as determined by AFM) is displayed in Figure 3A and 3B, respectively. In this study, nanotriangles were synthesized on a glass substrate using nanospheres (D = 400 nm) and 50.0 nm of Ag metal. After nanosphere removal (in Figure 3B), the samples were placed in a high vacuum chamber where they were thermally annealed for 1 h at ~600 °C. The nanotriangles (a = 114 nm, b = 54 nm) were converted into nanohemispheres (a = 110 nm, b = 61 nm) during this process. In both cases, the samples were stabilized in solvent and exposed to the appropriate molecular solution. In all cases, incubation in 11-MUA and $Cu(ClO_4)_2$ constitutes one layer. It is evident that even at low multilayer thicknesses, the nanotriangles give larger LSPR responses than the nanohemispheres. This result is consistent with studies done on identically prepared samples where the LSPR shift induced from hexadecanethiol was larger for nanotriangles than for nanohemispheres.[27] Additionally, theoretical studies support that as nanoparticles become more

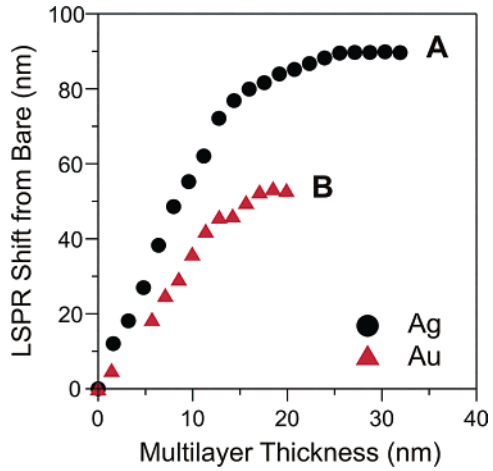

Figure 4. Composition dependence on the long range LSPR distance dependence. (A) LSPR shift vs layer thickness for Ag nanoparticles (a = 70 nm, b = 50.0 nm). (B) LSPR shift vs layer thickness for Au nanoparticles (a = 70 nm, b = 50.0 nm). Multilayer thicknesses were adjusted for SAM packing differences on Au and Ag. All extinction measurements were collected in a N_2 environment.

spherical, the electromagnetic field strength at their surface decreases.[23,52] This indicates that the electromagnetic fields at the nanoparticle surface are more intense for nonhemispherical nanoparticles. Additionally, because nanotriangles exhibit larger total LSPR shifts and can detect molecules larger distances away from the nanoparticle surface, their electromagnetic fields strength and sensing volumes are both larger.

Composition Influences on the LSPR Shifts Induced by Multilayer Adsorbates. An example of how the composition of the nanoparticles influences the LSPR sensor is found in Figure 4. In this case, nanosphere masks with a diameter, D = 280 nm, were created on glass substrates. Ag and Au nanoparticles (a = 70 nm) were created by depositing 50.0 nm of the desired metal onto the samples. The resulting nanoparticles had identical shapes and volumes but differed only in their compositions. After one SAM layer, the Ag sample (Figure 4A) gave larger LSPR shifts than the Au sample (Figure 4B). After 17 nm of multilayer thickness, the Au LSPR nanosensor stops responding. This adsorbate thickness produces approximately 52 nm LSPR shift from the plasmon of the bare sample. This result varies drastically from Ag nanoparticles with identical shapes and sizes. As seen in Figure 4A, the sensor response for the Ag nanosensor stops shifting after 26 nm of adsorbate layers. This is almost 10 nm thicker than the saturation thickness on Au. Additionally, the overall LSPR shift from bare Ag nanoparticles is almost 90 nm, nearly 40 nm greater than the Au sample. These results demonstrate that the electromagnetic fields surrounding the Ag nanoparticles are more intense and extend a greater distance from the surface than those surrounding the Au nanoparticles.

Height Influences on the LSPR Shifts Induced by Multilayer Adsorbates. Because NSL derived nanoparticles have extremely controllable deposition mass thicknesses, the effect of changing the nanoparticles' height for a fixed composition, shape, and in-plane width is easily explored. Figure 5A shows the LSPR shifts for multilayer adsorbates on Ag nanoparticles with in-plane widths of 100 nm and out-of-plane heights of (Figure 5A-1) 30 nm, (Figure 5A-2) 50 nm, and (Figure 5A-3) 70 nm. As the height is increased, the overall maximum LSPR shift decreases. In fact, for every 10 nm increase in nanoparticle height, the maximum LSPR shift decreases by ~15 nm (Figure 5B). This indicates that the overall magnitude of the electromagnetic fields extending from shorter nanoparticles is greater than for taller nanoparticles. Additional information can be learned regarding how nanoparticle height influences the sensing volume or how far away from the surface molecules can be sensed from the nanoparticle. Figure 5C shows that as the nanoparticle height is increased by 10 nm, the distance a molecule can be sensed from the surface drops by only 1.6 nm. This effect is not as pronounced as that seen for overall LSPR magnitude shifts.

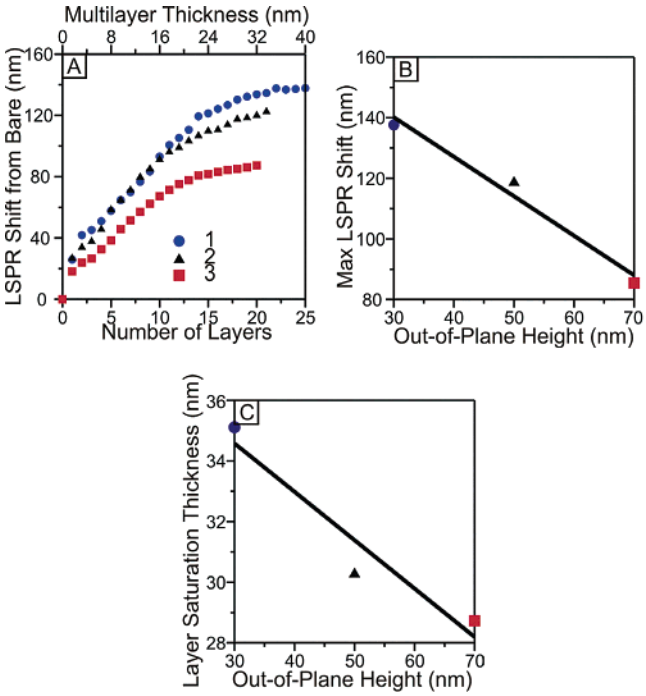

Figure 5. Out-of-plane height dependence on the long range LSPR distance dependence for Ag nanoparticles (D = 400 nm, a = 100 nm). (A) LSPR shift vs number of SAM layer thickness for Ag nanoparticles with b = (1) 30.0 nm, (2) 50.0 nm, and (3) 70.0 nm. All extinction measurements were collected in a N_2 environment. (B) Trends in the maximum LSPR shift vs out-of-plane width of Ag nanoparticles. Linear regression was used to fit the data to a line described by the following equation: $y = -1.30(x) + 179.2$. (C) Trends in the layer thickness saturation vs out-of-plane height of Ag nanoparticles. Linear regression was used to fit the data to a line described by the following equation: $y = -0.16(x) + 39.4$.

Width Influences on the LSPR Shifts Induced by Multilayer Adsorbates. Because the width of a NSL derived nanoparticle is controlled by the diameter of the nanosphere mask, the effect of changing nanoparticle width for a fixed composition, shape, and height is easily evaluated. Figure 6A shows the LSPR shifts for multilayer adsorbates on Ag nanoparticles with out-of-plane heights of 50 nm and in-plane widths of (Figure 6A-1) 70 nm, (Figure 6A-2) 78 nm, and (Figure 6A-3) 100 nm. As the nanoparticle width is increased, the overall maximum LSPR shift increases. In fact, for every 10 nm increase in nanoparticle width, the maximum LSPR shift increases by ~10 nm (Figure 6B). This indicates that the overall magnitude of the electromagnetic fields extending from wider nanoparticles are greater than for narrower nanoparticles. Additional information can be learned regarding how nanoparticle width influences the sensing volume or how far away from the surface molecules can be sensed from the nanoparticle. Figure 6C shows that as the nanoparticle width is increased by 10 nm, the distance a molecule can be sensed from the surface increases by 1.4 nm. This effect is slight when it is compared to the change seen for overall LSPR magnitude shifts.

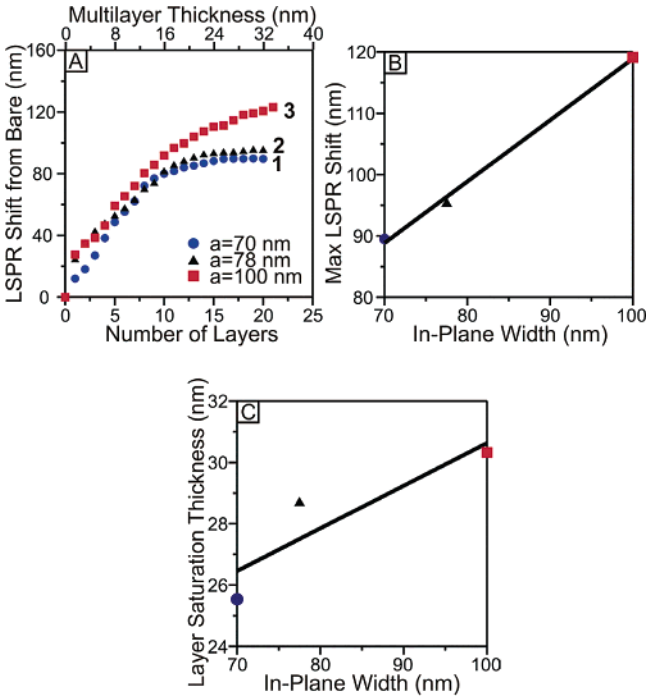

Figure 6. In-plane width dependence on the long range LSPR distance dependence for Ag nanoparticles ($b = 50.0$ nm). (A) LSPR shift vs number of SAM layer thickness for Ag nanoparticles with $a =$ (1) 70 nm, (2) 78 nm, and (3) 100 nm. All extinction measurements were collected in a N_2 environment. (B) Trends in the maximum LSPR shift vs in-plane width of Ag nanoparticles. Linear regression was used to fit the data to a line described by the following equation: $y = 1.00(x) + 18.8$. (C) Trends in the layer thickness saturation vs in-plane width of Ag nanoparticles. Linear regression was used to fit the data to a line described by the following equation: $y = 0.14(x) + 16.7$.

Aspect Ratio, Surface Area, and Volume Comparisons. The information presented in Figures 5 and 6 clearly follow linear height and width trends, respectively. These arguments could possibly collapse into one argument such as changes in nanoparticle surface area, volume, or aspect ratio. By plotting the maximum overall LSPR shifts and multilayer saturation thickness versus the three aforementioned parameters, interesting results were revealed. It was suspected that as the surface area of the nanoparticles increased, the total number of adsorbate molecules would increase thus providing a linear relationship between the saturation thickness and maximum LSPR shifts. Careful analysis showed that this hypothesis was not valid. Instead, two other relationships were revealed. For a fixed nanoparticle width, the maximum LSPR shift and sensing volume decreased with increasing nanoparticle surface area. For a fixed nanoparticle height, however, the maximum LSPR shift and sensing volumes increased for increasing nanoparticle surface area. Similar trends were revealed for nanoparticle volume measurements. This indicated that neither surface area nor volume were valid interpretations to the data. Aspect ratio comparisons yielded much different results. As the aspect ratio of the nanoparticles increased, the values for both saturation thickness and maximum LSPR peak shifts increased. While this trend could be used to describe these data, the results are better described by analyzing them as two distinct sets (fixed height with increasing width and fixed width with increasing height). In both the saturation thickness and maximum LSPR shift cases, trends for nanoparticles with fixed heights and increasing widths were approximately twice as responsive or had two times the slope in comparison to nanoparticles with varying height with fixed widths. Clearly, this analysis indicates that while the aspect ratio provides a valid description of the data, describing the results in terms of one fixed and one variable nanoparticle dimension provides more insight into the data. This interpretation is supported by results from theory,[52] which show that for spheroidal shaped particles, the plasmon resonance wavelength depends only on aspect ratio in the quasistatic approximation, but also depends on particle size when finite wavelength effects (radiative damping and depolarization) are taken into account.

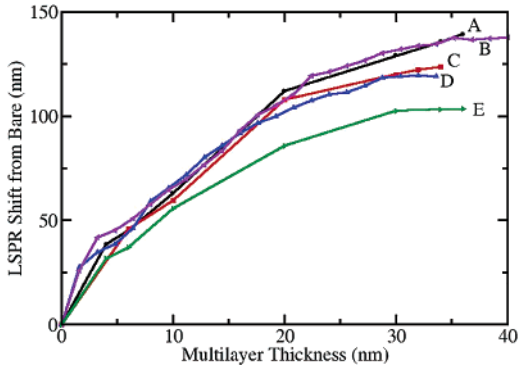

Figure 7. Shift of the LSPR from bare nanoparticles for both calculations and experiment. (A) Calculation for $a = 100$ nm, $b = 30$ nm nanoparticle for $n = 1.65$. (B) Experiment $a = 100$ nm, $b = 30$ nm nanoparticle. (C) Calculation $a = 100$ nm, $b = 50$ nm nanoparticle for $n = 1.65$. (D) Experiment $a = 100$ nm, $b = 50$ nm nanoparticle. (E) Calculation for $a = 100$ nm, $b = 30$ nm nanoparticle with $n = 1.50$.

Theory. To model the experiment results presented above, we used the discrete dipole approximation (DDA) method,[53,54] which is a finite element−based approach to solving Maxwell's equations for light interacting with an arbitrary shape/composition nanoparticle, to calculate the plasmon wavelength as a function of layer thickness. Bare silver nanoparticles with a truncated tetrahedral shape were first constructed from cubical elements and then multilayers of the adsorbate were added to the exposed surfaces of the nanoparticle to define the multilayer system. All calculations refer to silver nanoparticles with a dielectric constant taken from Lynch and Hunter.[55] The thickness of each monolayer in these studies is equal to the DDA grid spacing of 2 nm. Although this does not match the experimental layer monolayer thickness, for multilayer simulations such details are not important as will be apparent from the results. Two choices of nanoparticle height, b, were considered, 30 and 50 nm, each for a perpendicular bisector of 100 nm.

The shift of the LSPR from the bare nanoparticle results for the two calculations are presented as a function of layer thickness in Figure 7 along with the experimental results for the $a = 100$ nm, $b = 30$ and 50 nm nanoparticle. The DDA results include results for both nanoparticle heights for a layer index of refraction, n, of 1.65, and results for the $a = 100$ nm, $b = 30$ nm nanoparticle for $n = 1.50$. The index of refraction of the layer material is not known, but the chosen values are representative of possible values, and in fact we see that they both match the experiments reasonably well, with the $n = 1.65$ results being somewhat closer.

The results in Figure 7 indicate almost quantitative agreement of theory and experiment. For the $a = 100$ nm, $b = 50$ nm nanoparticle, the shift of the peak from bare nanoparticle is 124 nm when the adsorbate thickness is 34 nm, while the corresponding experimental result is 120 nm. For the $a = 100$ nm, $b = 30$ nm nanoparticle, the shift increases to 139 nm in the calculations and 137 nm in the experiments, for an adsorbate thickness of 35 nm. The results also indicate that the variation of the plasmon shift with layer thickness matches what is

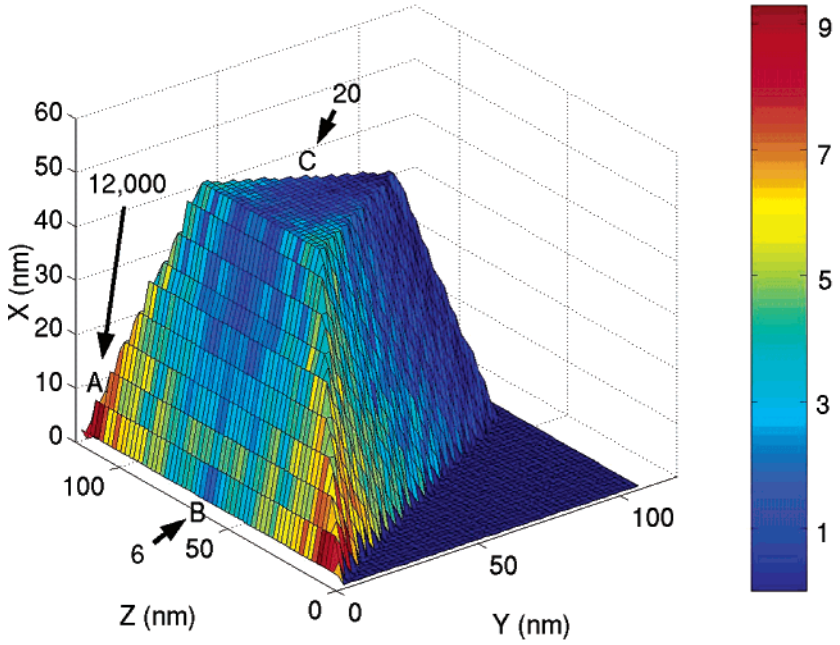

Figure 8. Plots of the logarithm of the square of the electric field averaged over distances between 0 and 2.0 nm from the surface (i.e., in the first adsorbed SAM/Cu^{2+} layer) for $a = 100$ nm, $b = 50$ nm nanoparticle. The numbers in the figure are relative to the incident light field, which is 1, so they are unitless.

measured. Some aspects of the curves in Figure 7 do not match perfectly; however, it is easy to imagine that the structural model we used is not completely right (for example, annealing effects in the layer structure have been ignored). However, the key conclusion is that theory confirms the observation that increasing the aspect ratio leads to larger plasmon resonance shifts and a larger saturation layer thickness.

To further explore the origin of the LSPR shift with layer thickness, we also calculated the electric field outside the nanoparticle for $a = 100$ nm, $b = 50$ nm, choosing the wavelength to be that associated with the plasmon maximum. Figure 8 shows the plots of the logarithm of square of the electric field, $|\mathbf{E}|^2$, for the first layer around the nanoparticle. The incident wavevector is perpendicular to the surface upon which the nanoparticle sits (not shown), and the polarization vector is parallel to the surface and along one edge of the nanoparticle, so the two hottest regions of the induced electric field occur at the two vertices associated with that edge. For most of the nanoparticle surface, the induced electric field is very small (comparable to the incident field) but near the vertices, $|\mathbf{E}|^2$ is as much as 12 000 times the incident field. Since the response of adsorbed layers is expected to be proportional to the local field, this suggests that the overall plasmon resonance shift arises from very uneven contributions from different parts of the nanoparticle. To further study the relationship between electric field and shift of the LSPR for different layer thickness, in Figure 9 we show the integrated electric field as a function of layer thickness for different points on the nanoparticle and for the average over the nanoparticle surface. In Figure 9, A, B, and C represent the electric field at the points A, B, and C shown in Figure 8, while D and E are the average electric field and experimental LSPR shift, respectively. The curves are normalized to have equal area in this comparison. We see that for the hottest part of the surface, point A, the electric field falls off very rapidly with distance from the surface, while for a cold part, for example, point C, the electric field decreases very slowly. The electric field curve at point B is somewhat between these two limits, and accidentally agrees with the experimental curve. The average over the surface agrees very well with the

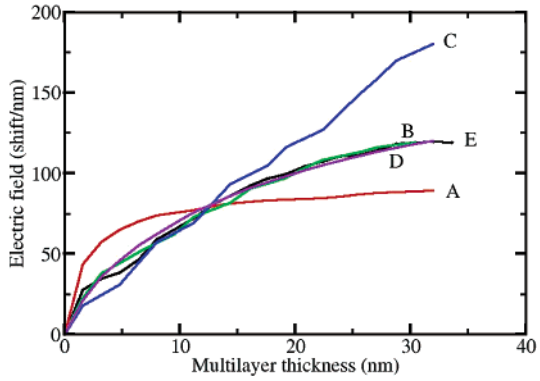

Figure 9. Integrated electric field $|\mathbf{E}|$ as a function of layer thickness of adsorbate. (A, B, and C) The electric field at points A, B, and C of the nanoparticle shown in Figure 7; (D) the averaged electric field; (E) the experimental LSPR shift.

experimental LSPR result, indicating that it is reasonable to assume that the fall-off of the LSPR wavelength with distance is a reflection of the behavior of the average E field. In addition, we see from Figure 9 that the hot spots dominate the average for distances close to the surface, while the cool spots play a dominant role for distances close to where the plasmon shift levels off. It should be noted that the leveling off of the plasmon resonance is more apparent than real. For larger layer thickness, our calculations show that there are Rayleigh scattering ($1/\lambda^4$) shifts and diffraction oscillations with layer thickness that extend indefinitely. However, these effects are cleanly separated from the more dramatic shifts that are seen in Figure 7 that are associated with the short distance (although here considered to be "long") behavior of the local field.

Surface Plasmon Resonance (SPR) versus LSPR Sensors. For ~20 years, surface plasmon resonance (SPR) sensors, that is, copper, gold, or silver planar films have been used as refractive index based sensors to detect analyte binding at or near a metal surface.[56] This sensor gains its sensitivity from an extremely large refractive index sensitivity ($\sim 2 \times 10^6$ nm/RIU) and modest decay length (200−300 nm),[57] and this sensitivity is proportional to the square of the electric field that extends

from the metal film. The overall response can be best described via the following equation:[57]

$$\Delta R = m\Delta n e^{-2d/l_d}(1 - e^{-2d/l_d}) \quad (1)$$

where ΔR is the wavelength shift response, m is the refractive index sensitivity, Δn is the change in refractive index induced by an adsorbate, d is the effective adsorbate layer thickness, and the l_d is characteristic electromagnetic field decay length. For planar SPR sensors, this equation quantitatively predicts an adsorbate's response. When applied to the LSPR nanosensor, this exponential equation approximates the response for adsorbate layers but does provide fully a quantitative explanation of its behavior. Similar to the SPR sensor, the LSPR nanosensor's sensitivity was realized to arise from the distance dependence of the average induced square of the electric field. This work provides important first steps in better explaining the LSPR sensor's response. Further analysis of the LSPR sensor using both experimental and theoretical approaches will help in the development of a mathematical expression to describe its wavelength response and is in progress.

Important differences to appreciate between the SPR and LSPR sensors are the comparative refractive index sensitivities and the characteristic electromagnetic field decay lengths. SPR sensors exhibit large refractive index sensitivities ($\sim 2 \times 10^6$ nm/RIU).[57] For this reason, the SPR response is often reported as changes in refractive index units. The LSPR nanosensor, on the other hand, has a modest refractive index sensitivity ($\sim 2 \times 10^2$ nm/RIU).[26] Given that this number is 4 orders of magnitude smaller for the LSPR nanosensor in comparison to the SPR sensor, initial assumptions were made that the LSPR nanosensor would be 10 000 times less sensitive than the SPR sensor. This, however, is not the case. In fact, the two sensors are very competitive in their sensitivities. The short (and tunable) characteristic electromagnetic field decay length provides the LSPR nanosensor with its enhanced sensitivity. These LSPR nanosensor results indicate that this decay length is $\sim 5-15$ nm or $\sim 1-3\%$ of the light's wavelength and depends on the size, shape, and composition of the nanoparticles. This differs greatly from the 200−300 nm decay length or $\sim 15-25\%$ of the light's wavelength for the SPR sensor.[57]

This work demonstrates the importance of the nanoscale phenomenon and their implication in sensing applications. Both the SPR and LSPR sensors operate on the principle that small changes in refractive index at or near a noble metal's surface can be used to detect analyte binding at very low concentrations. While the sensors gain their sensitivities via different mechanisms, their overall sensitivities are approximately equivalent. Further work will be done to develop a quantitative analysis for adsorbed materials on the LSPR nanosensor.

IV. Conclusions

The principal discovery reported here is that the long range distance dependence of the LSPR nanosensor is nonlinear and can be tuned by changing the composition, shape, in-plane widths, and out-of-plane heights of the nanoparticles. Because NSL allows the user to control the aforementioned characteristics, their influences on the maximum LSPR shift and maximum adsorbate thickness can easily be monitored using UV−vis spectroscopy. It was shown that using nanotriangles instead of nanohemispheres, Ag instead of Au, or larger aspect ratio nanoparticles, can increase the sensing volume of the nanoparticles. Additionally, information regarding the strength of the local electromagnetic fields surrounding the individual nanoparticles can be drawn. In particular, we demonstrated that the plasmon resonance shift close to the nanoparticle surface is dominated by hot spots while that farther away arises from colder regions around the nanoparticle surface. By comparing the overall maximum LSPR shifts of the nanoparticles, it was shown that increasing the aspect ratio of Ag nanotriangles produces larger plasmon resonances shifts and shorter ranged interactions.

Looking into the future, we expect these results to have important implications for all nanoparticle based optical sensors. These results directly apply to the design and optimization of LSPR chemical and biological nanosensors. By creating a sensor sample to best "fit" a given sized biomolecule at a certain distance from the nanoparticle surface, the optical response seen for that analyte can be optimized. Because the goal in many bioassays is to detect extremely low abundance of molecules, the difference between an optimized and unoptimized sensor could have a huge impact on its limit of detection.

Acknowledgment. The authors gratefully acknowledge support from the Nanoscale Science and Engineering Initiative of the National Science Foundation under NSF Award Number EEC-0118025. Any opinions, findings, and conclusions or recommendations expressed in this material are those of the authors and do not necessarily reflect those of the National Science Foundation. A. Haes also wishes to acknowledge the American Chemical Society Division of Analytical Chemistry and Eastman Chemical and Dupont for fellowship support.

References and Notes

(1) Benedek, G.; Martin, T. P.; Pacchioni, G. *Elemental and Molecular Clusters*; Springer Series in Materials Science; Springer-Verlag: Berlin, 1988; Vol. 6.
(2) Alivisatos, A. P. *J. Phys. Chem.* **1996**, *100*, 13226.
(3) Alivisatos, A. P. *Science* **1996**, *271*, 933.
(4) Brus, L. E.; Szajowski, P. F.; Wilson, W. L.; Harris, T. D.; Schuppler, S.; Citrin, P. H. *J. Am. Chem. Soc.* **1995**, *117*, 2915.
(5) Reed, M. A.; Kirk, W. P. *Nanostructures and Mesoscopic Systems*; Academic Press, Inc.: San Diego, CA, 1991.
(6) *Clusters and Colloids From Theory to Applications*; Schmid, G., Ed.; VCH Publishers: Weinheim, Germany, 1994; p 555.
(7) Steigerwald, M. L.; Brus, L. E. *Acc. Chem. Res.* **1990**, *23*, 183.
(8) Sundaram, M.; Chalmers, S. A.; Hopkins, P. F.; Gossard, A. C. *Science* **1991**, *254*, 1326.
(9) Storhoff, J. J.; Elghanian, R.; Mirkin, C. A.; Letsinger, R. L. *Langmuir* **2002**, *18*, 6666.
(10) Schneider, B. H.; Dickinson, E. L.; Vach, M. D.; Hoijer, J. V.; Howard, L. V. *Biosens. Bioelectron.* **2000**, *15*, 597.
(11) Zhang, H.-L.; Evans, S. D.; Henderson, J. R.; Miles, R. E.; Shen, T.-H. *Nanotechnology* **2002**, *13*, 439.
(12) Hutter, E.; Fendler, J. H.; Roy, D. *J. Phys. Chem. B* **2001**, *105*, 11159.
(13) Gu, Z.; Horie, R.; Kubo, S.; Yamada, Y.; Fujishima, A.; Sato, O. *Angew. Chem.* **2002**, *41*, 1153.
(14) Felidj, N.; Aubard, J.; Levi, G.; Krenn, J. R.; Salerno, M.; Schider, G.; Lamprecht, B.; Leitner, A.; Aussenegg, F. R. *Phys. Rev. B* **2002**, *65*, 075419/1.
(15) Haynes, C. L.; Van Duyne, R. P. *J. Phys. Chem. B* **2001**, *105*, 5599.
(16) Mulvaney, P. *MRS Bull.* **2001**, *26*, 1009.
(17) El-Sayed, M. A. *Acc. Chem. Res.* **2001**, *34*, 257.
(18) Link, S.; El-Sayed, M. A. *J. Phys. Chem. B* **1999**, *103*, 8410.
(19) Kreibig, U.; Gartz, M.; Hilger, A.; Hovel, H. Optical investigations of surfaces and interfaces of metal clusters. In *Advances in Metal and Semiconductor Clusters*; Duncan, M. A., Ed.; JAI Press Inc.: Stamford, CT, 1998; Vol. 4, p 345.
(20) Mulvaney, P. *Langmuir* **1996**, *12*, 788.
(21) Kreibig, U. Optics of nanosized metals. In *Handbook of Optical Properties*; Hummel, R. E., Wissmann, P., Eds.; CRC Press: Boca Raton, FL, 1997; Vol. II., p 145.
(22) Kreibig, U.; Gartz, M.; Hilger, A. *Ber. Bunsen-Ges.* **1997**, *101*, 1593.
(23) Jensen, T. R.; Kelly, K. L.; Lazarides, A.; Schatz, G. C. *J. Cluster Sci.* **1999**, *10*, 295.

(24) Hulteen, J. C.; Van Duyne, R. P. *J. Vac. Sci. Technol., A* **1995**, *13*, 1553.
(25) Jensen, T. R.; Schatz, G. C.; Van Duyne, R. P. *J. Phys. Chem. B* **1999**, *103*, 2394.
(26) Malinsky, M. D.; Kelly, K. L.; Schatz, G. C.; Van Duyne, R. P. *J. Am. Chem. Soc.* **2001**, *123*, 1471.
(27) Haes, A. J.; Van Duyne, R. P. *J. Am. Chem. Soc.* **2002**, *124*, 10596.
(28) Riboh, J. C.; Haes, A. J.; McFarland, A. D.; Yonzon, C. R.; Van Duyne, R. P. *J. Phys. Chem. B* **2003**, *107*, 1772.
(29) McFarland, A. D.; Van Duyne, R. P. *Nano Lett.* **2003**, *3*, 1057.
(30) Raschke, G.; Kowarik, S.; Franzl, T.; Sonnichsen, C.; Klar, T. A.; Feldmann, J. *Nano Lett.* **2003**, *3*, 935.
(31) Walczak, M. M.; Chung, C.; Stole, S. M.; Widrig, C. A.; Porter, M. D. *J. Am. Chem. Soc.* **1991**, *113*, 2370.
(32) Iler, R. K. *J. Colloid Interface Sci.* **1966**, *21*, 569.
(33) Clark, S. L.; Hammond, P. T. *Adv. Mater.* **1998**, *10*, 1515.
(34) Lvov, Y.; Essler, F.; Decher, G. *J. Phys. Chem.* **1993**, *97*, 13773.
(35) Lvov, Y.; Haas, H.; Decher, G.; Mohwald, H.; Mikhailov, A.; Mtchedlishvily, B.; Morgunovva, E.; Vainshtein, B. *Langmuir* **1994**, *10*, 4232.
(36) Decher, G.; Hong, J. D.; Schmitt, J. *J. Thin Solid Films* **1992**, *210*−*211*, 831.
(37) Kleinfeld, E. R.; Ferguson, G. S. *Mater. Res. Soc. Symp. Proc.* **1995**, *369*, 697.
(38) Kleinfeld, E. R.; Ferguson, G. S. *Chem. Mater.* **1995**, *7*, 2327.
(39) Kleinfeld, E. R.; Ferguson, G. S. *Science* **1994**, *265*, 370.
(40) Lvov, Y.; Ariga, K.; Ichinose, I.; Kunitake, T. *Langmuir* **1996**, *12*, 3038.
(41) Kotov, N. A.; Dekany, I.; Fendler, J. H. *J. Phys. Chem.* **1995**, *99*, 13065.
(42) Kotov, N. A.; Dekany, I.; Fendler, J. H. *Adv. Mater.* **1996**, *8*, 637.
(43) Keller, S. W.; Kim, H. N.; Mallouk, T. E. *J. Am. Chem. Soc.* **1994**, *116*, 8817.
(44) Feldheim, D. L.; Crabar, K. C.; Natan, M. J.; Mallouk, T. E. *J. Am. Chem. Soc.* **1996**, *118*, 7640.
(45) Schmitt, J.; Decher, G.; Dressik, W. J.; Branduo, S. L.; Geer, R. E.; Shashidhal, R.; Calvert, J. M. *Adv. Mater.* **1997**, *9*, 61.
(46) Hatzor, A.; Weiss, P. S. *Science* **2001**, *291*, 1019.
(47) Evans, S. D.; Ulman, A.; Goppert-Berarducci, K. E.; Gerenser, L. J. *J. Am. Chem. Soc.* **1991**, *113*, 5866.
(48) Bharathi, S.; Nogami, M.; Ikeda, S. *Langmuir* **2001**, *17*, 7468.
(49) Freeman, T. L.; Evans, S. D.; Ulman, A. *Langmuir* **1995**, *11*, 4411.
(50) Evans, S. D.; Flynn, T. M.; Ulman, A. *Langmuir* **1995**, *11*, 3811.
(51) Evans, S. D., Personal Communication, 2003.
(52) Zeman, E. J.; Schatz, G. C. *J. Phys. Chem.* **1987**, *91*, 634.
(53) Draine, B. T.; Flatau, P. J. *J. Opt. Soc. Am. A* **1994**, *11*, 1491.
(54) Kelly, K. L.; Coronado, E.; Zhao, L.; Schatz, G. C. *J. Phys. Chem. B* **2003**, *107*, 668.
(55) Lynch, D. W.; Hunter, W. R. In *Handbook of Optical Constants of Solids*; Palik, E. D., Ed.; Academic Press: New York, 1985; p 350.
(56) Brockman, J. M.; Nelson, B. P.; Corn, R. M. *Annu. Rev. Phys. Chem.* **2000**, *51*, 41.
(57) Jung, L. S.; Campbell, C. T.; Chinowsky, T. M.; Mar, M. N.; Yee, S. S. *Langmuir* **1998**, *14*, 5636.